EurJIC
European Journal of Inorganic Chemistry

A Journal of ChemPubSoc Europe

Accepted Article

Title: New Boron(III) blue emitters for all-solution processed OLEDs: molecular design assisted by theoretical modeling

Authors: Cristian A.M. Salla, Jéssica Teixeira dos Santos, Giliandro Farias, Adailton J. Bortoluzi, Sergio F. Curcio, Thiago Cazati, Róbert Izsák, Frank Neese, Bernardo de Souza, and Ivan Bechtold

To be cited as: *Eur. J. Inorg. Chem.* 10.1002/ejic.201900265

Link to VoR: http://dx.doi.org/10.1002/ejic.201900265

WILEY-VCH

10.1002/ejic.201900265

New boron(III) blue emitters for all-solution processed OLEDs: molecular design assisted by theoretical modeling

Cristian A. M. Salla[a], Jéssica Teixeira dos Santos[b], Giliandro Farias[b], Adailton J. Bortoluzi[b], Sergio F. Curcio[c], Thiago Cazati[c], Róbert Izsák[d], Frank Neese[d], Bernardo de Souza[b]*, Ivan H. Bechtold[a]*

[a]Physics Department, Universidade Federal de Santa Catarina, 88040-900 Florianópolis, SC, Brazil

[b]Chemistry Department, Universidade Federal de Santa Catarina, 88040-900 Florianópolis, SC, Brazil

[c]Physics Department, Universidade Federal de Ouro Preto, 35400-000 Ouro Preto, MG, Brazil

[d]Max-Planck-Institut für Kohlenforschung, Kaiser-Wilhelm-Platz 1, 45470 Mülheim an der Ruhr, Germany

*Email: ivan.bechtold@ufsc.br; tel: +55 48 37212304

bernardo.souza@ufsc.br; tel: +55 48 37213608

Graphical Abstract

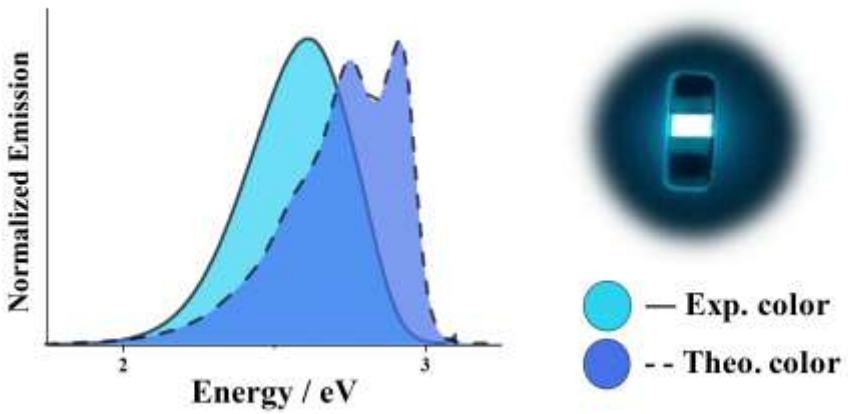

We investigate the emission and photophysics from known and new boron(III) complexes, by both experiments and theory. Within our theoretical framework, we show to be possible to determine the actual color of emission and predict the fluorescence rates. Solution processed OLEDs were also built from those, with good efficiency and potential for application, also displaying the predicted colors.

Abstract

Luminescent boron (III) complexes have recently been employed as emitters in organic light emitting diodes (OLEDs) with reasonable success. They are easy to prepare and sufficiently stable to be used in such devices, being of great interest as a simple molecular emissive layer. Although emitters for this class with all colors have already been reported, highly efficient and stable blue emitters for applications in solution processed devices still pose a challenge. Here, we report the design, synthesis and characterization of new boron complexes based on the 2-(benzothiazol-2-yl)phenol ligand (HBT), with different donor and acceptor groups responsible for modulating the emission properties, from blue to red. The molecular design was assisted by calculations using our newly developed formalism, where we demonstrate that the absorption and fluorescence spectra can be successfully predicted, being a powerful technique to evaluate molecular photophysical properties prior to synthesis. In addition, density functional theory (DFT) allows to understand the molecular and electronic structure of the molecules in greater detail. The molecules studied here presented fluorescence efficiency as high as $\Phi = 0.88$ and all-solution processed OLEDs were prepared and characterized under ambient atmosphere, after dispersion in the emitting layer. Surprisingly, even considering these rather simple experimental conditions, the blue emitters displayed superior properties compared to present literature, in particular with respect to the current efficiency stability.

Keywords: boron(III) complexes; theoretical modeling; blue emitters; solution processed OLEDs; DFT.

1. Introduction

There has been significant progress in recent years in the design of new materials for application in OLEDs, particularly for those emitting in the blue region. Despite the improvements with phosphorescence and thermally activated delayed fluorescence (TADF), fluorescent blue materials have proven to be the best option so far for the construction of efficient, stable and long-lived devices in displays and lighting systems.[1] Most current research involving blue emitters deal with classical scaffolds with known good fluorescence yields such as anthracene, pyrene, and fluorene. However, the possibility of excimer formation through packing usually leads to reduced electroluminescent efficiency and degradation of color purity in such devices.[2] In that context, the color tuning of four-coordinate organoboron compounds achieved by modifying ligands provides an alternative for the development of new blue emitters.[3][4] Even so, there are only a few reports on both

efficient and stable blue fluorescent complexes and very little on the theoretical modeling of the emission dynamics.

Boron (III) complexes have been extensively studied in recent years by different research groups. These compounds are widely employed in organic synthesis,[5] chemical biology[6] and material sciences,[7] mainly due to versatility, ease of synthesis, physicochemical stability and low cost.[8] In particular, luminescent organoboron complexes have received considerable attention in the development of efficient OLEDs[9] because of their high emission quantum yield, good thermal stability and their charge carrier properties.[10] Devices based on these materials with emissions from blue to red,[11] white[12] and near infrared[13] have already been reported. In addition, these materials can be processed in solution to make thin films or dispersed on host materials, which simplifies the manufacturing process and reduces the production costs.[10,14]

The type of ligand and the nature of substituent groups on either the ligands or the boron center itself influences the photophysical properties of these compounds, which are affected by the boron–chromophore interaction. In particular, ligands with flat and rigid π-conjugated skeletons are useful for obtaining luminescent complexes for OLED applications, since they minimize the decay through non-radiative pathways.[15,16] Boron dypyrromethene complexes (BODIPYs) are among the most well-known boron complexes with an intense fluorescence and tunable emission wavelengths of this class. Nevertheless, in general, BODIPYs and their derivatives exhibit self-quenching due to the small Stokes shifts and tight packing, reducing their emission efficiency in solid state, which has limited their potential application in OLEDs.[17] Trying to overcome these limitations, boron (III) complexes with the widely used ligand 2-(benzothiazol-2-yl)phenol (HBT)[18] were recently synthesized. They displayed high Stokes shifts and high fluorescence intensities at the same time, and their emission color was shown to be tunable through chemical modifications on the aromatic moiety.[19]

Herein, we report the design, synthesis and characterization of a series of emissive neutral boron (III) complexes (Figure 1) based on the HBT ligand containing different donor and acceptor groups, where the luminescent properties could be modulated, leading from blue to red emitters. Calculations using DFT assisted molecular and electronic structure interpretation, as well as some excited state dynamics. We show that our recently developed formalism[19] in conjunction with time-dependent density functional theory (TD-DFT), allows the prediction of emissive rates and the fluorescence spectra with impressive accuracy. Finally, the complexes were dispersed on a double-host emissive layer and all-solution

processed OLEDs were prepared. The device constructed from the blue emitter with the highest fluorescence quantum yield (Φ = 0.88), prepared under normal ambient conditions, revealed itself to be one of the most efficient all-solution processed devices based on boron complexes known to date.

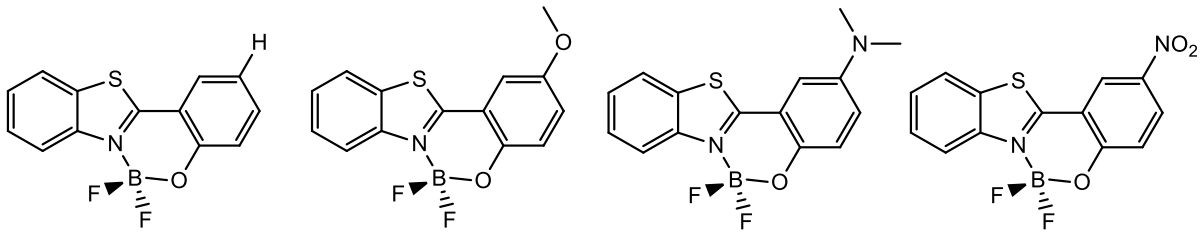

B1 **B2** **B3** **B4**

Figure 1. Proposed structures of synthesized Boron(III) complexes.

2. Results and Discussion

2.1 Synthesis of the ligands and complexes

The HBT derivatives can be synthesized in a one-pot procedure, starting from commercially available 2-aminobenzenethiol and substituted phenols in ethanol, using hydrogen peroxide as oxidant. Then, the difluoroboron complexes **B1**-**B4** can be prepared from the respective ligand, by treatment with boron trifluoride diethyl ether in the presence of DIPEA. All of the complexes were obtained from direct crystallization in dichloromethane and for the nitro substituted compound (**B4**), single crystals were obtained. A synthetic route for the ligands and the boron complexes is shown in Scheme 1 and Schemes 1S – 3S.

2.2 Crystal structure and geometries from DFT

The molecular structure of complex **B4** was determined by single crystal X-ray diffraction studies. As can be seen in Figure 2, the boron(III) center adopts a typical tetrahedral geometry, binding with N1 and O1 of HBT and two fluorine atoms. Bond distances and angles are reported at the Supporting Information and are similar to those of other related organoboron compounds previously reported.[10, 20] The molecule crystallizes in a $P2_1/c$ space group with four molecules per lattice and between these units, a π-stacking interaction is observed with a shorter distance between centroids of 3.615 Å and coplanarity angle of 1.78º.

10.1002/ejic.201900265

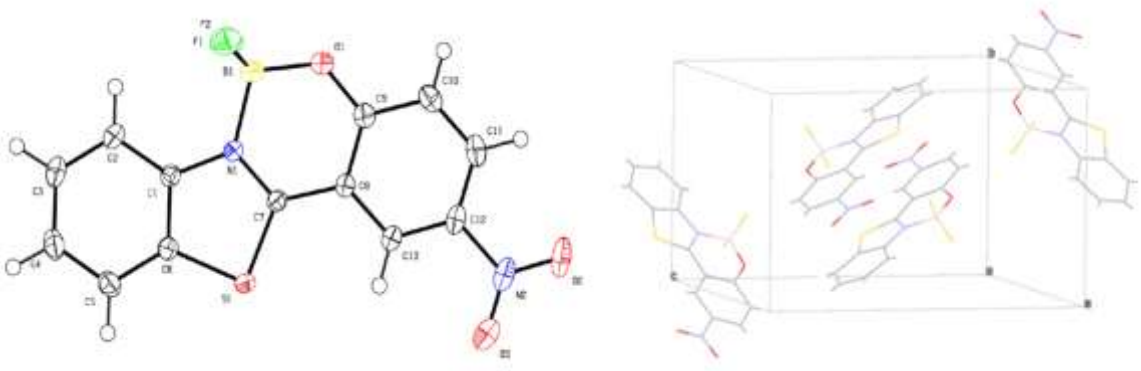

Figure 2. ORTEP representation of the molecular structure of complex **B4** (left) and packing structure (right).

Unfortunately, despite their high purity, we could not obtain single crystals for the other complexes. In the absence of accurate experimental data for **B1**, **B2** and **B3**, we decided to rely on quantum chemistry and optimized the geometries using DFT at the PBE0/def2-TVZP(-f) level. Figure 3 shows that the calculated structures around the boron center are quite similar for all complexes. The vibrational frequencies confirm that the geometries correspond to a minimum on the potential energy surface, since no negative frequencies were found. For the complex **B2** with a methoxy group, two isomers were considered by rotating the C-O bond, with an energy increase of 0.693 kcal mol^{-1} from **B2a** to **B2b**. Table 3S of Supporting Information compares the crystalline structure parameters of **B4** with the optimized theoretical calculations for **B1-B4**. As can be seen, the theoretical geometry for **B4** is in good agreement with the experiment, where the average error for bond lengths was 0.83% and 1.23% for bond angles, which supports further use of PBE0 in subsequent investigations.

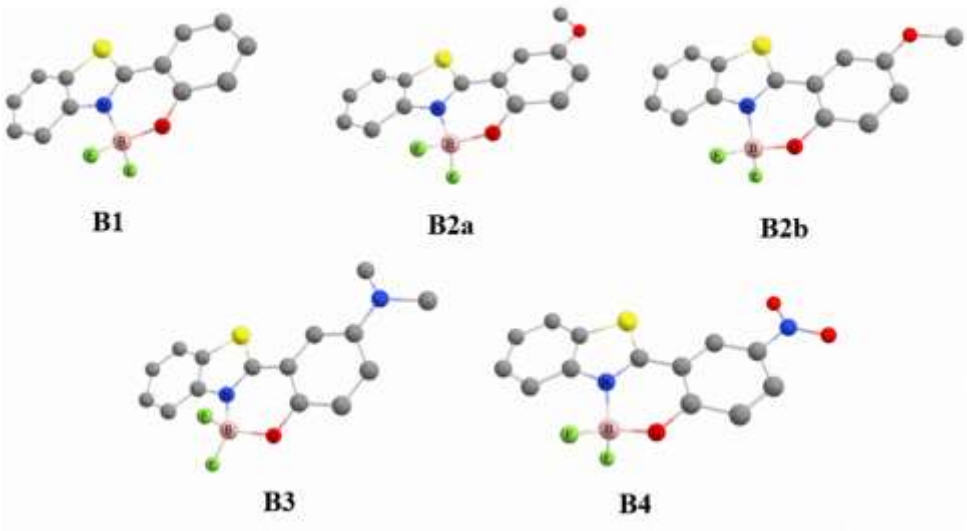

Figure 3. Optimized geometry for complexes **B1-B4** obtained from DFT using PBE0/def2-TZVP(-f).

2.3 Photophysical Properties

The UV-Vis absorption and emission spectra of complexes **B1-B4** obtained in CH_2Cl_2 are presented in Figure 4 and summarized in Table 1. All complexes exhibited an intense absorption band around 300 nm, and lower energy absorption bands with maxima between 360 and 460 nm, which are commonly attributed to $\pi \rightarrow \pi^*$ transitions of the HBT ligand. These were strongly affected by the substituent groups: the bands of **B2** and **B3,** containing electron donor groups, were red shifted when compared with **B1** (without substituent), while those for **B4**, which has an electron withdrawing group, were blue shifted.

The emission peaks of the complexes **B1**, **B2** and **B4** after excitation at the lower energy peak were located in the blue and green region, with maxima centered at 424, 481 and 502 nm. **B3**, with the dimethylamine group, exhibited the lowest energy emission band (595 nm), already suggesting a smaller HOMO-LUMO gap. This indicates possibility of modulating the emission maxima with a simple modification of the molecular structure. The results in the solid state, with complexes dispersed in a PMMA matrix, are similar to those obtained in solution and can be seen in Figure 7S.

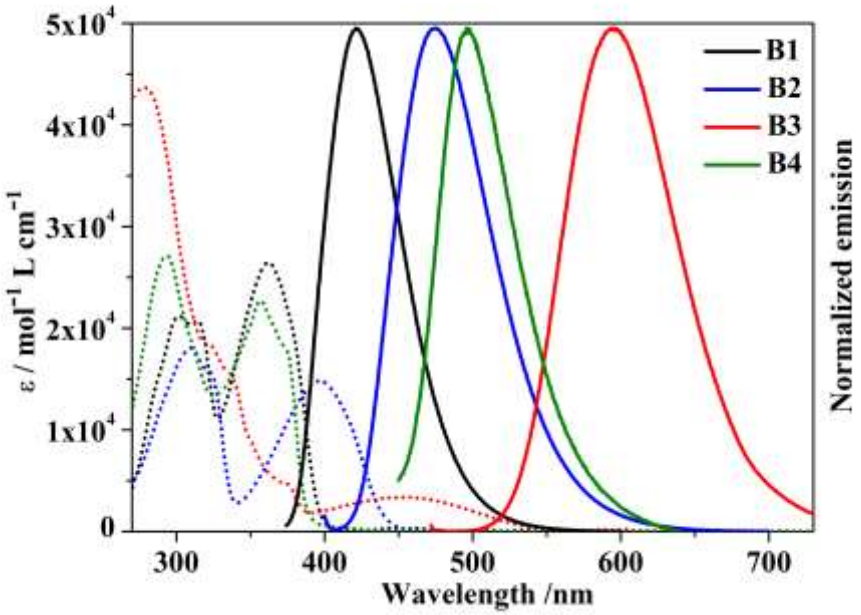

Figure 4. Optical absorption (dotted line) and emission (solid line) spectra of the boron (III) complexes in CH_2Cl_2 solution 2.0×10^{-5} mol L^{-1}. Emission spectra were obtained by excitation at the low energy region of the first absorption.

Excited state decay curves of the boron complexes were collected at the wavelength of maximum emission in solution, indicating lifetimes typical of fluorescence, in the range of

nanoseconds (Figure 9S). The fluorescent decay curves for **B1** and **B3** in solution could be fitted with a mono-exponential function, resulting in a lifetime of 1.4 ns and 15.8 ns, respectively, as expected for monomeric emission. The fluorescent decay curves of **B2** in solution was best fitted with a bi-exponential function displaying two distinct lifetimes in solution, 9.7 ns and 5.7 ns, with 51.8% and 48.2% contribution to the total emission. These agree with the fact that there are two conformers for **B2**. In order to confirm the individual emission of both isomers, the lifetime was collected at 445 nm and 505 nm, that is, 30 nm bellow and above the maximum emission wavelength, where a variation of each contribution is expected due to distinct emission bands. In both cases, the same two lifetimes (9.7 ns and 5.7 ns) were observed, with contributions of 27.8% and 72.2% for 455 nm, and 68.6% and 31.4% for 505 nm, thus confirming the existence of the isomers absorbing at different wavelengths. The **B4** excited state decay curve in solution could only be fitted satisfactorily with a triexponential function, resulting in lifetimes of 8.4 ns (7.1%), 1.6 ns (16.5%) and 0.2 ns (76.4%), possibly due to emission from aggregates even at very low concentrations.

When the absolute emission quantum yield was measured, a quite high photoluminescence quantum yield (PLQY, Φ_F) was obtained for complex **B2** (Φ_F = 0.88 in CH_2Cl_2), followed by complex **B3** (Φ_F = 0.45 in CH_2Cl_2), both of which contain donor groups. The lowest PLQY was observed for complex **B4** (Φ_F = 0.02 in CH_2Cl_2). This demonstrates the significant role of the substituents on the luminescent properties of HBT-FB complexes when compared to complex **B1** (Φ_F = 0.26 in CH_2Cl_2), without any substituent. The solid-state luminescence properties followed the same pattern, with only a reduction on the **B2** and **B3** PLQY (see Table 1), which can be due to the existence of strong interchromophore π-π interactions in the solid state, leading to larger nonradiative rates.[10] The emission of **B4** was too low even to allow proper quantification.

Table 1. Photophysical data for the boron (III) complexes.

	Solution[a]				**Solid State**		
	λ_{abs} (nm)/ ε (M^{-1} cm^{-1})	**λ_{em} (nm)**	**Φ_F[b]**	**τ_S (ns)[c]**	**λ_{abs} (nm)**	**λ_{em} (nm)**	**Φ_F[b]**
B1	362 /26484	421	0.26	1.4	363	424	0.26
B2	396/15984	475	0.88	8.3[d]	397	481	0.53
B3	449/485	595	0.45	5.4	454	576	0.37
B4	356/22416	496	0.02	15.8[d]	355	502	-

[a] In CH_2Cl_2 at 2.0×10^{-5} mol L^{-1}. [b] The uncertainty in the Φ_F measure was ±0.01. [c] ± 0.1 ns. [d] $\tau = \Sigma \tau_i^2 A_i / \Sigma \tau_i A_i$, due to multi-exponential profile.

2.4 Theoretical Modeling of the Electronic Structure and Fluorescence

To have a better understanding of the electronic and luminescent properties of **B1-B4**, we first carried out calculations using DFT on all complexes. The calculated HOMO (-1), HOMO, LUMO and LUMO (+1) are shown in Figure 5, with their energies on the vertical axis. As can be seen, the HOMO increases in energy from **B1** to **B3**, as the donating power of the substituent increases, and decreases in **B4**, while the LUMO energy does not change significantly. For the complexes **B1-B3**, the HOMO has major contributions from the phenol part of the chelate ligands, and has a small contribution from the benzothiazole moiety, particularly for **B1** and **B2**, whereas the LUMO for these complexes is mostly a π* orbital spread throughout the ligand. In addition, the HOMO (-1) and LUMO (+1) are quite similar for these species, being a delocalized π orbital and a π* centered on the heterocycle.

In contrast, the electronic structure of **B4** is different. For this complex, the HOMO is more evenly spread throughout the ligand and the LUMO is centered on both the π* orbitals of the C-N bond of the thiadiazol ring and the nitro group. The HOMO (-1) for this complex is centered on the benzothiazole and the LUMO (+1) on the phenol moiety, demonstrating that the substituents can have a significant impact on energy levels and charge distribution, which ultimately influences the radiative rates and color, as shown later on.

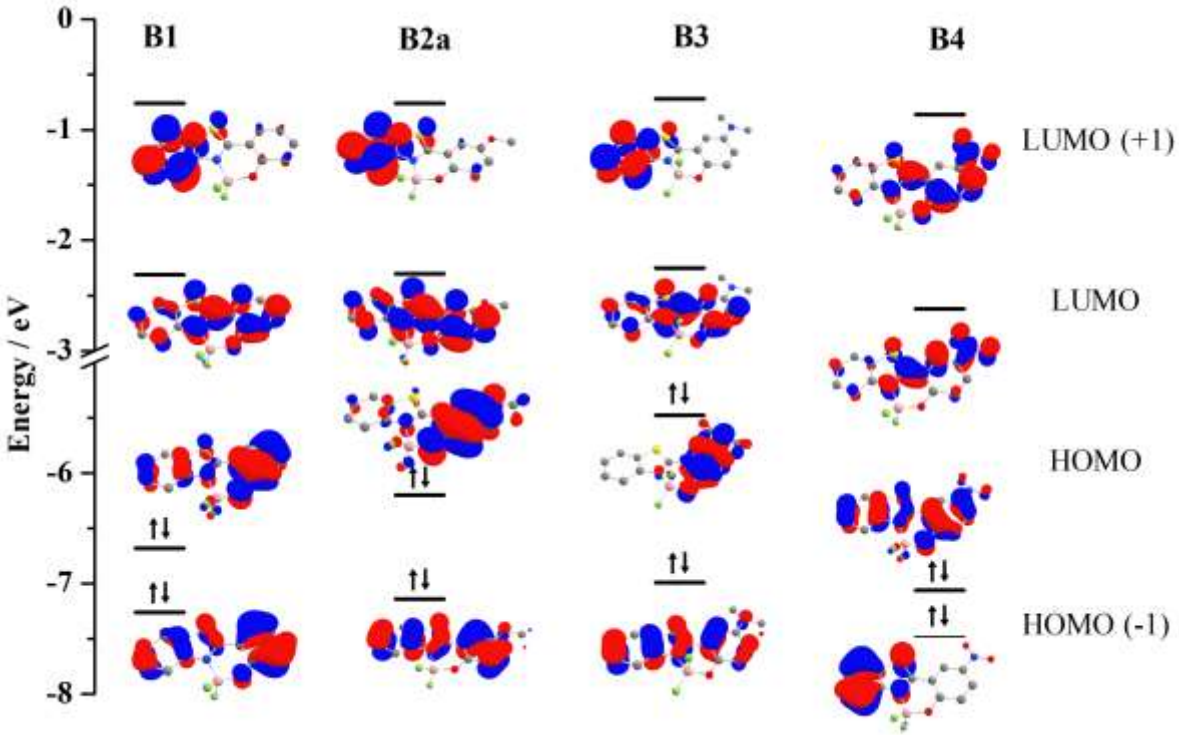

Figure 5. Frontier molecular orbitals of complexes **B1-B4** calculated using PBE0/def2-TZVP(-f).

The electronic excitations were modeled by TD-DFT, using linear response CPCM to account for the solvent effect on the energy, and the calculated absorption spectra as well as convoluted gaussians reproducing the experimental spectra are shown for each molecule in Figure 6, along with the experimental results. After specifying the number of Gaussians to be used in the fitting by selecting prominent peaks and shoulders on the experimental spectra, the width and intensity of the curves were allowed to vary to achieve the best fit. Allowing the width to vary may account for broadening due to vibrational progressions, which is why some features of the spectra were not selected for fitting. While owing to the nature of this process and the possible failings of the TD-DFT method some electronic transitions may be missed or misidentified, a tentative assignment is still possible between the Gaussians and the TD-DFT transition state labels. Table 4S displays some of the most intense calculated transitions, with the corresponding largest excitation amplitudes. There are three intense transitions predicted for compounds **B1-B3** and the lowest energy transition of all these complexes can be assigned as HOMO→LUMO. Furthermore, the higher-energy transitions in Table 4S and Figure 6 are similar for both **B2** isomers, but the low energy ones have slightly different energies, indicating that the experimental spectrum might have contributions from both species. This also suggests distinct emission bands, as was observed by time-resolved fluorescence measurements. On the other hand, the complex **B4**, as expected from the molecular orbital analysis, has a different profile for the electronic transitions. Its state of lowest energy, which without the CPCM correction is the fifth singlet state, results from a mixed HOMO→LUMO (70%) and HOMO→LUMO (+1) (21%) configuration with a transition dipole moment much smaller than that found for the first excitation of **B1-B3**. The other high energy transitions are similar to those of the previous complexes. Comparisons of the theoretical and experimental oscillator strengths and energy values are shown in Table 2, and the band assignment from these are shown in Figure 6.

10.1002/ejic.201900265

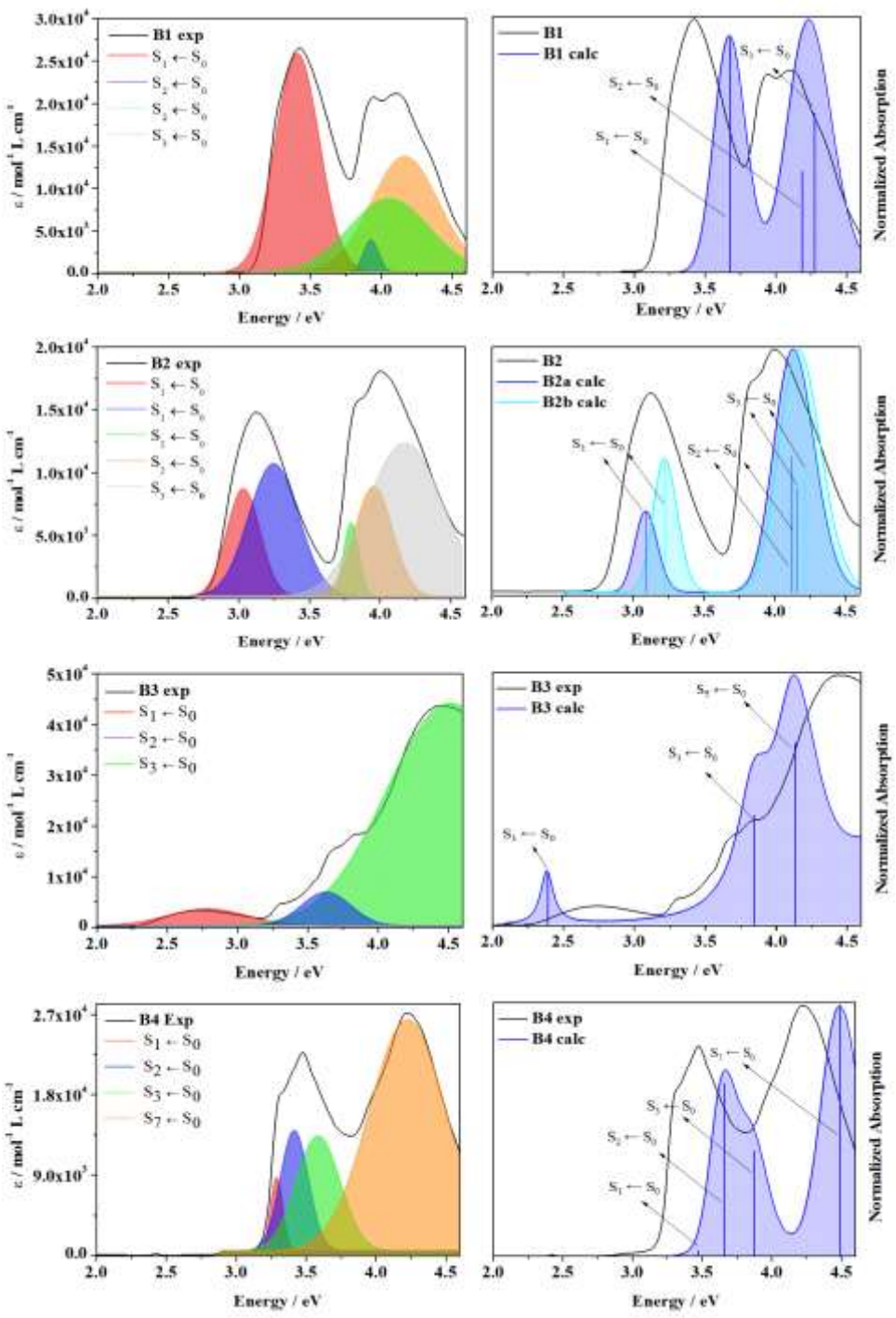

Figure 6. Experimental absorption spectra of **B1-B4** in CH_2Cl_2 (left, with tentative assignments) and the theoretical absorption spectra (right) calculated using PBE0/def2-TZVP(-f) and convoluted with Gaussians of 0.2 eV width.

Since fluorescence generally occurs from the lowest excited state to the ground state, and its rate depends on the transition matrix element of the dipole moment operator, it is important to discuss its variation as a function of the molecular structure. The transition dipole moment can be rationalized as a function of the charge redistribution during the

electronic transition which is directly affected by the substituents. From the frontier natural transition orbitals (NTOs) in Figure 8S, for **B1-B3**, the excitation occurs mainly from the phenol ring to the π* orbitals of the C-N bond, and can be classified as a charge transfer-like transition. The presence of donating groups contributes to delocalizing the HOMO around the phenol moiety and ends up decreasing the charge transfer character of the excitation (since there are phenol components also in the LUMO), thus lowering the transition dipole moment associated with it. For **B4**, the much smaller transition dipole moment is clearly due to a larger delocalization of both the HOMO and LUMO, particularly centering the LUMO (+1) around the phenol ring (see **B1-B3** in Figure 5), thus giving rise to a more π-π*-like transition.

Table 2. Comparison between experimental and calculated vertical energy differences and oscillator strengths using PBE0/def2-TZVP(-f).

Experiment		**Theory**	
Energy / eV	***f*** [a]	**Energy (S_n) / eV**	***f***
		B1	
3.42	0.3422	3.68 (S_1)	0.3862
3.94	0.0199	4.18 (S_2)	0.1675
4.07	0.2191		
4.18	0.2829	4.23 (S_3)	0.2615
		B2 (a / b)	
3.04	0.0908	3.09 / 3.23 (S_1)	0.2092 / 0.2885
3.25	0.1660		
3.80	0.0297	4.12 / 4.14 (S_2)	0.3514 / 0.2602
3.97	0.1047		
4.18	0.2720	4.15 / 4.20 (S_3)	0.2692 / 0.2711
		B3	
2.76	0.0844	2.38 (S_1)	0.1124
3.64	0.1024	3.79 (S_2)	0.0058
		3.84 (S_3)	0.2311
4.52	1.4597	4.12 (S_5)	0.3825
		4.24 (S_6)	0.1082
		4.45 (S_7)	0.0051
		4.65 (S_8)	0.0968
		B4	
3.23	0.0311	3.46 (S_1)	0.0101
3.49	0.1789	3.65 (S_2)	0.3726
4.14	0.1194	3.86 (S_3)	0.2262

		3.86 (S_4)	0.0172
4.20	0.6277	4.49 (S_7)	0.5391

[a] $f = 4.32\times10^{-9}\int\varepsilon d\sigma$.

The radiative rates (k_r) and fluorescence spectra were also calculated for all complexes using our newly developed approach. [19] The PBE0 and B2PLYP functionals were chosen to calculate adiabatic electronic energy differences on top of the PBE0 geometries and Hessians. The calculated rates are displayed in Table 3 and showing that experimental and theoretical values are in very good agreement. Even for **B2**, the k_r is correctly predicted to be the average of both isomers. As the radiative rate diminishes along with the transition dipole moment for **B2** and **B3,** the increase of the emission yield seems to occur due to a smaller non-radiative rate. Nevertheless, we could predict that the quantum yield would be at least of the same order from the k_r, regardless of the change in emission color.

Table 3. Experimental and calculated rate constants in CH_2Cl_2 using the def2-TZVP(-f) basis set.

	k_r(exp) × 10^8 (s^{-1})[a]	k_r(theo) × 10^8 (s^{-1}) PBE0[b]	k_r(theo) × 10^8 (s^{-1}) B2PLYP[b]	k_{nr}(exp) × 10^8 (s^{-1})[c]
B1	1.85	2.23	2.51	5.28
B2	1.06	0.99 (**B2a**) 1.38 (**B2b**)	0.85 (**B2a**) 1.08 (**B2b**)	0.14
B3	0.83	0.01	0.98	1.01
B4	0.01	0.04	0.04	0.62

[a] $k_r = \Phi / \tau$. [b]using def2-TZVP(-f). [c]$k_{nr} = (1 - \Phi) / \tau$.

The emission spectra, presented in Figure 7, are also coherent with the experimental results. The main vibrational progression is due to the C=C and C=N stretching modes, from the energy separation of these peaks of about 0.15 eV (1200 cm^{-1}). We also calculated the theoretical observed color and, as one can verify from the areas below the lines, we can predict them with good agreement to the experiment. The larger error was found in **B4**, where we could not reproduce the green color of emission due to the 0-0 energy difference error, a known issue in DFT.[21] That particular color deviation comes from the fact that the energy gap was on the border of green and blue and the small shift induced a larger error on the color perceived. In general, the B2PLYP functional that has a fraction of MP2 correlation performed better, predicting better energy differences as expected from previous results. [19]

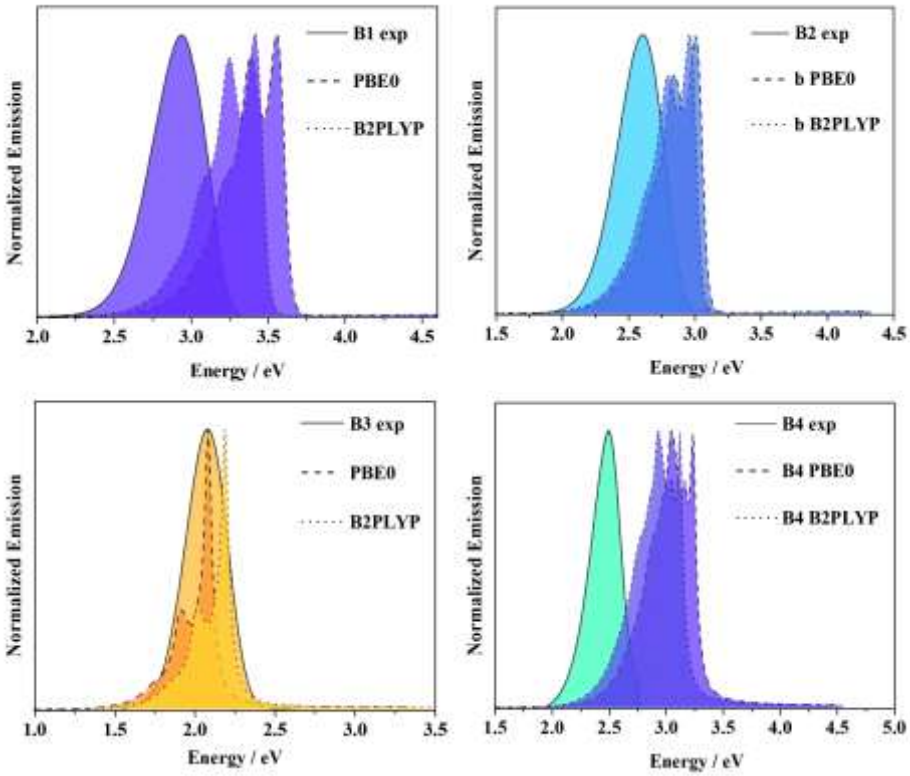

Figure 7. Experimental and predicted emission spectra using PBE0 and the B2PLYP functionals using the def2-TZVP(-f) basis. The colors of the areas represent the actual emission colors obtained from the spectra and the color matching functions.

2.5 Thermal and Electrochemical Properties

A thermogravimetric analysis (TGA) of **B1–B4** under nitrogen atmosphere revealed that the initial decomposition temperatures are 171, 254, 298 and 104 °C (see Figure 10S). Such thermal stability indicates that all the complexes can undergo thermal treatments until at least 100 °C and that both **B2** and **B3** could even be sublimated in evaporated OLEDs. Cyclic voltammetry in CH_2Cl_2 solutions were performed to estimate the HOMO and LUMO energy levels from the oxidation and reduction potentials. Figure 11S shows the cyclic voltammograms and Table 4 summarizes the electrochemical data. Complexes **B1** and **B4** exhibited irreversible oxidation, **B2** showed a quasi-reversible oxidation and **B3** reversible oxidation peaks. It was found that the substituent effect agrees with the shifts in the UV-Vis spectra. The complex **B4,** with the electron withdrawing group, presented the lowest HOMO and LUMO energy, while **B3,** with the strongest electron donating group, had the highest HOMO and LUMO. The HOMO and LUMO energies obtained from voltammetry agree with the tendency from DFT, also confirming the substituent effect on these orbital energies.

Table 4. Electrochemical properties of complexes **B1-B4**.

	E_{ox} (V)	E_{red} (V)	E_{HOMO} (eV)[a]	E_{LUMO} (eV)[a]	Bandgap (eV)[b]
B1	-	-1.69	-6.22	-3.11	3.11
B2	1.16	-	-5.96	-3.14	2.82
B3	0.54	-	-5.34	-3.07	2.27
B4	-	-1.16	-6.82	-3.64	3.20

[a] Determined from peak potentials, where $E_{HOMO} = -(4.8 + E_{ox})$ and $E_{LUMO} = -(4.8 - E_{red})$.[22]

[b] Calculated from the onset of the absorption spectra in solution.

2.6 Electroluminescent Properties

The electroluminescence (EL) properties of the complexes were then evaluated in all-solution processed devices with a simple structure: ITO/Pedot:PSS(25 nm)/TcTA:OXD-7:**BX**(25 nm)/PFNBr:TEAB(35 nm)/CsF(1.3 nm)/Al(100 nm), with **BX**=**B1**, **B2** or **B3**. The thickness of the organic layers was determined with atomic force microscopy, which also presented mean surface roughness lower than 0.70 nm, see Fig. 12S in supporting information. **B4** was not used in the electroluminescent layer due to the low PLQY. A co-host system containing TcTA:OXD-7 (7:3 in Wt) as both hole and electron transport layer was conveniently chosen according to the singlet energy levels to favor energy transfer to the guest, adequate charge carrier transport and balance inside the emitting layer (EML), as well as good thin film formation.[23] The PFNBr:TEAB was used as an electron transporting layer (ETL). The total energy diagrams and electrical properties of the OLEDs build from **B1-B3** are presented in Figure 8 and the results are summarized in Table 5.

Devices with **B1-B3** have a turn-on potential around 4 V mainly due to the high charge injection barriers. The one containing the **B2-**emitter performed best overall, which can be mainly attributed to the high PLQY, with maximum values of luminance (L), current efficiency (CE) and external quantum efficiency (EQE), 357.10 cd m^{-2}, 0.39 cd A^{-1} and 0.20 % respectively. The latter performance is superior to and more stable than some of the recently reported evaporated devices[8, 14] and it is among the best known for all-solution processed devices using boron complexes up to date, if not the best (see Table 5S). Usually, the TcTA:OXD-7 co-host system is ideal for phosphorescent guests, especially green and red.[24] However, here it was found promising also for blue fluorescent guests, with good resulting efficiency. It is important to stress that the devices were processed and characterized under ambient conditions, which intrinsically reduced their performance. Atomic force microscopy images of the EML (see Figure 12S) suggest that **B3** forms agglomerates, possibly due to dissolution problems and this may have impaired its performance.

10.1002/ejic.201900265

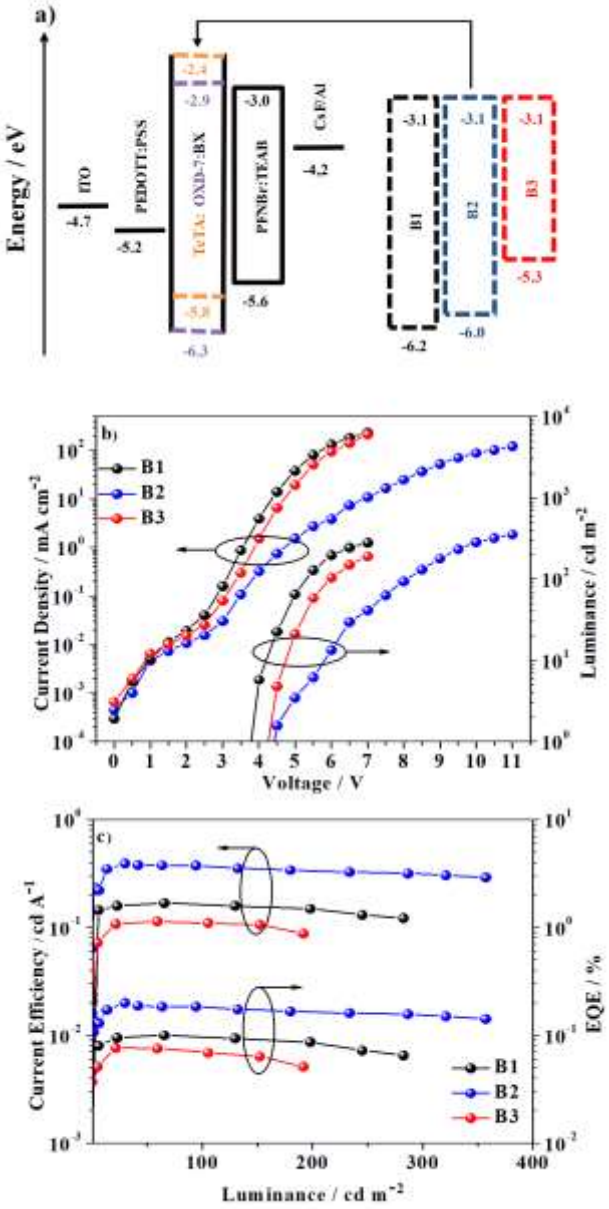

Figure 8. (a) Energy diagram and **B1-B3** OLED characteristics. (b) current density and luminance vs. voltage. (c) current efficiency and external quantum efficiency vs. luminance. The arrows indicate the y-labels corresponding to the curves.

Table 5. Electrical characterization and electroluminescence parameters for the OLEDs **B1-B3**.

	V_{on} (V)[a]	L_{max} (cd m^{-2})	CE_{max} (cd A^{-1})	EQE_{max} (%)
B1	3.80	282.30	0.17	0.10
B2	4.39	357.10	0.39	0.20
B3	4.27	191.70	0.11	0.07

[a] Defined as the voltage at which a luminance of 1 cd m^{-2} was achieved.

The electroluminescence spectra and color coordinates of the devices at maximum luminance are presented in Figure 9. Here, the emission has bands centered at 462, 478 and 587 nm for devices with **B1**, **B2** and **B3**, respectively. The shoulder at 430 nm observed for the **B3**-device corresponds to the regular PFNBr emission.[25] A lack of an energy barrier to block holes sometimes allows recombination in ETL and favors emission at these wavelengths. The EL peaks associated with **B2** and **B3** agree with solid-state emission while for **B1** a red shift of about 30 nm was observed. The CIE (Commission Internationale de l'Eclairage, $CIE_{x,y}$) for the devices using **B1**-**B3** are (0.21;0.28), (0.21;0.29) and (0.51;0.41), indicating that the compounds can be of interest for constructing white light emitting devices for lighting systems.[26]

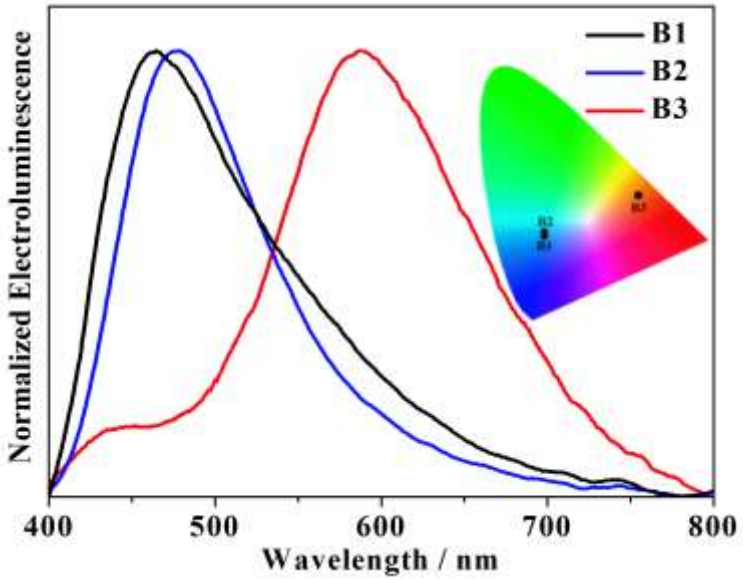

Figure 9. Normalized EL spectra and $CIE_{x,y}$ of OLEDs **B1-B3.**

3. Conclusion

The design, synthesis and characterization of a new series of boron complexes with the HBT ligand was presented. Their emission properties could be modulated by inserting donor and acceptor groups, leading to emission in the blue, green and red regions. Calculations in conjunction with excited state lifetime measurements confirmed that the complex with a methoxy donor group (**B2**) adopts two isomeric conformations, being a strong blue emitter with very high PLQY (0.88). These compounds exhibited good thermal stability as well as HOMO and LUMO energy levels appropriate for application in OLEDs. Surprisingly, when casted as an emissive layer in all-solution processed OLEDs prepared and characterized under ambient conditions, they demonstrated a superior performance compared to others already reported, in particular concerning the current efficiency stability. We also wish to highlight

the potential of the theoretical formalism used to predict the rates, spectra and actual fluorescence color of such complexes. That demonstrates the capability of the technique to assist molecular design by predicting photophysical properties prior to the actual synthesis.

4. Experimental Section

4.1 General Procedures

All starting materials were purchased from Aldrich, Acros, Merck or Vetec and were used without further purification.

The measurements of carbon, hydrogen and nitrogen percentages for ligands and the synthesized complexes were performed on a C, H, N - Perkin-Elmer 2400 elemental analyzer. The spectra in the infrared region were obtained in a Perkin Elmer Spectrum 100 spectrophotometer, in the region of 4000 to 450 cm^{-1}. The method of attenuated total reflectance (ATR) was used to analyze all samples. The ^{1}H NMR spectra of the ligands were obtained with a Bruker FT-NMR 200 MHz spectrophotometer and a Bruker FT-NMR Ascend 400 MHz spectrophotometer. Hydrogen chemical shifts were recorded in ppm units using tetramethylsilane (TMS, δ = 0.00 ppm) as internal reference and deuterated DMSO, acetone or chloroform as the solvent.

4.2 Synthesis and Characterization

All ligands used were synthesized and purified according to literature methods.[10, 20,27, 28] The synthesis of the complexes **B1**, **B2**, **B3** and **B4** is described in Scheme 1. In a round bottom flask the corresponding hydroxybenzothiazole (1.0 mmol) and *N*,*N*'-diisopropylethylamine (DIPEA, dry) (0.25 mL) were dissolved in dry dichloromethane (10.0 mL) under an inert atmosphere. Then trifluoride diethyl ether ($BF_3.Et_2O$) (1.0 mL) was added dropwise at room temperature. Precipitation began immediately. After one hour, the resulting solid was filtered and washed with cold dichloromethane. The crude product was purified with crystallization in dichloromethane. All the complexes were characterized by infrared, ^{1}H NMR, ^{13}C NMR, melting point and elemental analysis, **B1** and **B3** are in agreement with the previously reports[10,20] and the data for **B2** and **B4** is shown in Figures 1S-6S.

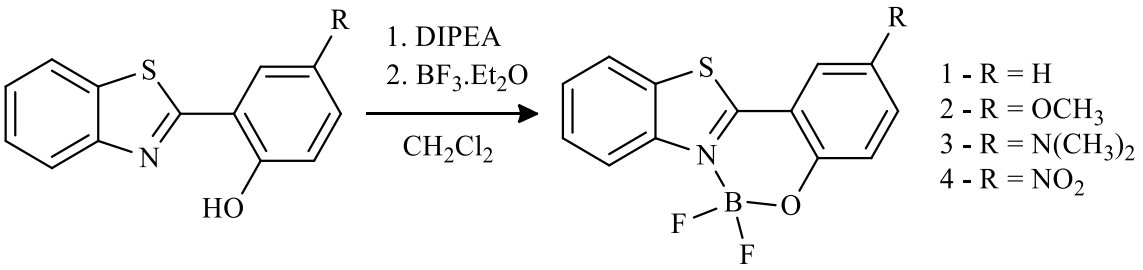

Scheme 1. Synthesis of **B1**-**B4** complexes.

B2. Green solid, 72% yield.

Mp: 290.9 - 271 °C. IR (ATR, cm^{-1}): υ (C-Har) 3080, υ (C-H) 2844, υ (C=C) 1572-1485, υ (C-N) 1324, υ (C-O-C) 1266-1035, υ (B-F) 1060, δ (C-Har) 757; ^{1}H NMR (200 MHz, acetone-d_6) δ/ppm: 8.31 (d, 2H); 7.80 (t, 1H); 7.71 (t, 1H); 7.35 (t, 1H), 7.32 (t, 1H); 7.11 (t, 1H); 3.90 (s, 3H); ^{13}C NMR (100 MHz, DMSO-d_6) δ/ppm: 164.9, 152.8, 151.9, 150.9, 135.2, 126.9, 125.5, 122.6, 122.4, 120.2, 119.1, 118.5, 111.6, 56.1; elemental analysis calcd. (%) for $C_{14}H_{10}BF_2NO_2S$: C 55.11, H 3.30, N 4.59; found: C 55.00, H 3.25, N 4.49.

B4. Pale green solid, 74 % yield.

Mp: 291.2 – 292.8 °C. IR (ATR, cm^{-1}): υ (C-Har) 3107, υ (C=C) 1579-1484, υ (N=O) 1508-1327, υ (B-F) 1055, υ (C-N) 841, δ (C-Har) 733; ^{1}H NMR (400 MHz, DMSO-d_6) δ/ppm: 9.17 (d, 1H); 8.28 (dd, 1H); 8.16 (dd, 2H); 7.58 (td, 1H); 7.49 (td, 1H); 7.27 (d, 1H); ^{13}C NMR (100 MHz, DMSO-d_6) δ/ppm: 161.7, 151.7, 140.5, 135.8, 128.5, 127.6, 127.1, 125.9, 124.8, 123.1, 122.6, 120.1, 118.1; elemental analysis calcd. (%) for $C_{13}H_7BF_2N_2O_3S$: C 48.78, H 2.20, N 8,75; found: C 48,63, H 2.28, N 8.46.

4.3 X-Ray Data Collection and Structure Determination

The X-ray diffraction analysis was performed on a Bruker APEX II DUO diffractometer using radiation generated by a molybdenum tube (MoKα λ = 0.71073 Å) and a graphite monochromator. During the analysis, the sample was sustained at 200K. Crystal structure was solved by direct methods and was refined by the least squares method with complete matrix, using the programs SIR97 and SHELXL-97 respectively.[29, 30] The graphical representations of the molecular structures were generated using the program PLATON.[31] The Supporting Information containing selected crystallographic data is available free of charge on the ACS Publications website. Full crystallographic tables (including structural factors) have been

deposited at the Cambridge Structural Database, as supplementary publication number CCDC 1872766. Copies of these data can be obtained free of charge at www.ccdc.cam.ac.uk.

4.4 Thermogravimetric Analysis and Cyclic Voltammetry Studies

The thermogravimetric analysis was performed with approximately 2 mg of sample in a platinum crucible, with a nitrogen flow of 100 mL min^{-1} and a heating ramp of 10 °C min^{-1} in a temperature range of 30-900 °C. The equipment used is of the brand Shimadzu, model TGA-50.

The redox behavior of the complexes was investigated by square wave voltammetry in a potentiostat-galvanostat BAS (Bioanalytical Systems, Inc.) model Epsilon. A concentration of 2.5×10^{-4} mol L^{-1} in a CH_2Cl_2 solution was used under nitrogen atmosphere. Tetrabutylammonium hexafluorophosphate (0.1 mol L^{-1}) was used as support electrolyte and the electrochemical cell was composed of three electrodes: work - vitreous carbon; auxiliary - platinum wire; reference - Ag/AgCl. For correction of the reference electrode, ferrocene ($E_{1/2}$ *vs* NHE = 398 mV) was used.

4.5 Spectroscopic Measurements

The electronic spectra in the ultraviolet, visible and near infrared regions were obtained for all the complexes in the range of 200−800 nm in a Perkin-Elmer spectrophotometer model Lambda-750. The values of ε are given in L mol^{-1} cm^{-1}. The emission spectra were obtained using a Varian Cary Eclipse Fluorescence spectrophotometer. The spectroscopy measurements were performed in CH_2Cl_2 solution and solid state using PMMA matrix containing 10% **B1**-**B4**. The analyses were performed using spectroscopic grade solvents, substrates and quartz cuvettes with a capacity of 1 mL and 1.00 cm of optical path at 25 ºC. Absolute quantum yields (Φ) were made using a Hamamatsu Photonics Absolute Quantum Yield Measurement System model c9920-02G which is based on the integrating sphere method.

Singlet-excited state photoluminescence decay curves were recorded using the time-correlated individual photon counting method of a FluoTime 200 (PicoQuant) spectrometer. The excitation was promoted using a 401 nm pulsed diode laser with repeating rates ranging from 5.0 to 20 MHz. Photoluminescence was collected perpendicular to the excitation and passed through a polarizer adjusted at the magic angle. The detection system consists of a monochromator and a multi-channel base photomultiplier (Hamamatsu R3809U-50). Lifetimes were obtained by fitting a convolution of the instrument's response function and a

sum of exponentials to the fluorescence data using the FluoFit® software. The residual plots and the chi-square (χ^2) were used to accurately determine the quality of the accessories during the analysis procedure.

4.6 Theoretical methods

Geometry optimizations of complexes **B1-B4** were carried out in vacuum, using the Orca 4.0.1 software package[32] at the DFT level using the PBE0[33][34] functional and the def2-TZVP(-f) basis set for all atoms. [35-37] Dispersion effects were included using Grimme's D3 correction with Becke-Johnson (BJ)[38,39] damping. The RIJCOSX algorithm[40,41] was employed to accelerate the evaluation of the functionals, using the resolution of identity approximation for the Coulomb part (RIJ), and the chain of spheres approach for the Fock exchange (COSX). RIJCOSX requires the specification of an auxiliary basis set for the Coulomb part and that of a numerical integration grid for the exchange part discussed elsewhere.[40,41] The vibrational frequencies computed on the optimized geometries of the complexes included no imaginary ones. TD-DFT was employed to obtain the first 10 singlet excited states, using the same calculation protocol to optimize the geometry and calculate the Hessian of the first excited state. Single point calculations using the B2PYLP functional were also performed[42] for the excitation energies, since it is supposed to give better results,[39] which was actually corroborated here as well. Images of the complex geometries were obtained using the Chemcraft program.[43]

In order to calculate the rates, the path integral approach recently developed and implemented by us in the ORCA_ESD module[19] was employed, using PBE0 Hessians and geometries for the ground and excited states in all cases. The line width was set to 300 cm^{-1} and the default Lorentzian line shape was used to achieve a better fit to experimental data. Also, all frequencies below 300 cm^{-1} were removed. The default options were used for all the other parameters. In order to include solvent effects in the excited state energies, the linear response conductor-like polarizable continuum model (LR-CPCM) was used while the regular CPCM was employed for the ground state. Since in the case of fluorescence, we already start at a properly solvated excited state, the actual dielectric constant of the medium was used in the energy correction expression instead of the square of the refractive index, as an approximation to the slow relaxation term. The colors were obtained from the spectra using the SPECTOCOLOR software, also developed by one of us locally. It uses analytic formulations of the CIE color matching functions [44] to convert from spectral data to several color spaces and can be obtained free of charge from https://github.com/bersouza/spectocolor.

4.7 OLED Device Fabrication

The OLEDs were prepared in ambient conditions on glass substrates coated with ITO (Delta technologies Co, 4-8 Ω) previously etched and cleaned in a detergent solution, deionized water, acetone and isopropanol, sequentially in an ultrasonic bath. The cleaned ITO glass was treated with UV/ozone for 5 min to adjust the work function and improve wetting. A film with 25 nm of poly(3,4-ethylenedioxythiophene)/poly(4-styrenesulfonate) (PEDOT:PSS) was spin-casted and then annealed at 160 °C for 30 min as hole-injection layer. Then the 25 nm-thick EML composed of Tris(4-carbazoyl-9-ylphenyl)amine (TcTA) and 1,3-bis[2-(4-tert-butylphenyl)-1,3,4-oxadiazo-5-yl]benzene (OXD-7) TcTA:OXD-7 (7:3) co-host were dissolved in trichloroethylene with 4 wt% of emitter B1-B3 complexes previously optimized, and was spin-coated and annealed at 60 °C for 10 min. Afterward, a 35 nm-thick ETL containing poly[(9,9-bis(3'-((N,N-dimethyl)-N-ethylammonium)-propyl)-2,7-fluorene)-alt-2,7-(9,9-dioctylfluoren)] dibromide (PFNBr) and tetraethylammonium bromide (TEAB) PFNBr:TEAB (10:3) dissolved in methanol:water (8:2) was spin-coated and annealed at 60 °C for 10 min.[45] Finally, 1.3 nm of cesium fluoride (CsF) as inject electron layer (IEL) and 100nm of Al as cathode was deposited in a high-vacuum thermal deposition system at a rate of 0.1 and 1.0 A s^{-1} at a base pressure of 1×10^{-6} Torr, respectively. The active area for all devices was about 4 mm^2 and the final device structure was ITO/Pedot:PSS (25 nm)/TcTA:OXD-7:**BX** (25 nm)/PFNBr:TEAB(35 nm)/CsF (1.3 nm)/Al (100 nm) with **BX=B1, B2** or **B3**.

The full characterization of the devices was realized using a Keithley Model 2400 source and a Hamamatsu Photonics Absolute Quantum Yield Measurement System model c9920-02G at ambient conditions without encapsulation. The thickness and morphological aspects of the thin films were determined with a Nanosurf Flex AFM, operating in tapping mode under ambient conditions with a scanning rate of 1.0 Hz and 512×512 pixels.[46]

Acknowledgements

The authors are grateful to CNPq (Proj. Univ. 401028/2016-0), FINEP, CAPES, FAPESC, INCT-INEO, H2020-MSCA-RISE-2017 (OCTA, #778158) and the Max Planck Gesellschaft for financial support. We are also grateful to Prof. Fernando R. Xavier for the ^{13}C NMR measurements.

References

[1] H. Kuma, C. Hosokawa, *Sci. Technol. Adv. Mater.* **2014**, 15, 034201.

[2] S. Lee, B. Kim, H. Jung, H. Shin, H. Lee, J. Lee, J. Park, *Dyes Pigm.* **2017**, 136, 255–261.

[3] T. M. H. Vuong, J. Weimmerskirch-Aubatin, J. Lohier, N. Bar, S. Boudin, C. Labbé, F. Gourbilleau, H. Nguyen, T. T. Dang, D. Villemin, *New J. Chem.* **2016**, 40, 6070–6076.

[4] Z. Zhang, Z. Zhang, H. Zhang, Y. Wang, *Dalton Trans.* **2017**, 47, 127–134.

[5] V. S. Sadu, H.-R. Bin, D.-M. Lee, K.-I. Lee, *Sci.Rep.* **2017**, 7, 242.

[6] D. B. Diaz, A. K. Yudin, *Nat. Chem.* **2017**, 9, 731–742.

[7] D. Frath, J. Massue, G. Ulrich, R. Ziessel, *Angew. Chem. Int. Ed. Engl.* **2014**, 53, 2290–2310.

[8] D. Suresh, B. Ferreira, P. S. Lopes, C. S. B. Gomes, P. Krishnamoorthy, A. Charas, D. Vila-Viçosa, J. Morgado, M. J. Calhorda, A. L. Maçanita, P. T. Gomes, *Dalton Trans.* **2016**, 45, 15603–15620.

[9] Y.-J. Shiu, Y.-T. Chen, W.-K. Lee, C.-C. Wu, T.-C. Lin, S.-H. Liu, P.-T. Chou, C.-W. Lu, I.-C. Cheng, Y.-J. Lien, Y.Chi, *J. Mater. Chem. C* **2017**, 5, 1452–1462.

[10] M. Santra, H. Moon, M.-H. Park, T.-W. Lee, Y. K. Kim, K. H. Ahn, *Chem. Eur. J.* **2012**, 18, 9886–9893.

[11] Q. D. Liu, M. S. Mudadu, R. Thummel, Y. Tao, S. Wang, *Adv. Funct. Mater.* **2005**, 15, 143–154.

[12] Y. Liu, J. Guo, H. Zhang, Y. Wang, *Angew. Chem. Int. Ed.* **2002**, 41, 182–184.

[13] M. Sassi, N. Buccheri, M. Rooney, C. Botta, F. Bruni, U. Giovanella, S. Brovelli, L. Beverina, *Sci. Rep.* **2016**, 6, 34096.

[14] D. Suresh, C. S. B. Gomes, P. S. Lopes, C. A. Figueira, B. Ferreira, P. T. Gomes, R. E. Di Paolo, A. L. Maçanita, M. T. Duarte, A. Charas, J. Morgado, D. Villa-Viçosa, M. J. Calhorda, *Chem. Eur. J.* **2015**, 21, 9133–9149.

[15] D.-H. Kim, A. D'Aléo, X. K. Chen, A. D. S. Sandanayaka, D. Yao, L. Zhao, T. Komino, E. Zaborova, G. Canard, Y. Tsuchiya, E. Choi, J. W. Wu, F. Fages, J. L. Brédas, J. C. Ribierre, C. Adachi, *Nat. Photonics.* **2018**, 12, 98–104.

[16] D. Suresh; P. S. Lopes, B. Ferreira, C. A. Figueira, C. S. B. Gomes, P. T. Gomes, R. E. Di Paolo, A. L. Maçanita, M. T. Duarte, A. Charas, J. Morgado, M. J. Calhorda, *Chem. Eur. J.* **2014**, 20, 4126–4140.

[17] Y. Zhou, J. W. Kim, M. J. Kim, W.-J. Son, S. J. Han, H. N. Kim, S. Han, Y. Kim, C. Lee, S.-J. Kim, D. H. Kim, J.-J. kim, J. Yoon, *Org. Lett.* **2010**, 12, 1272–1275.

[18] J. S. García, F. Maschietto, M. Campetella, I. Ciofini, *J. Phys. Chem. A* **2018**, 122, 375–382.

[19] B. de Souza, F. Neese, R. Izsák, *J. Chem. Phys.* **2018**, 148, 034104.

[20] X. Li, Y.-A. Son, *Dyes Pigm.* **2014**, 107, 182–187.

[21] C. A. Guido, S. Knecht, J. Kongsted, B. Mennucci, *J. Chem. Theory Comput.* **2013**, 9, 2209–2220.

[22] I. Seguy, P. Jolinat, P. Destruel, J. Farenc, R. Mamy, H. Bock, J. Ip, T. P. Nguyen, *J. Appl. Phys.* **2001**, 89, 5442–5448.

[23] J.-H. Jou, S. Kumar, A. Agrawal, T.-H. Li, S. Sahoo, *J. Mater. Chem. C* **2015**, 3, 2974–3002.

[24] K. S. Yook, J. Y. Lee, *Adv. Mater.* **2014**, 26, 4218–4233.

[25] S. Ohisa, T. Kato, T. Takahashi, M. Suzuki, Y. Hayashi, T. Koganezawa, C. R. McNeill, T. Chiba, Y.-J. Pu, J. Kido, *ACS Appl. Mater. Inter.* **2018**, 10, 17318–17326.

[26] S. Reineke, M. Thomschke, B. Lüssem, K. Leo, *Rev. Mod. Phys.* **2013**, 85, 1245–1293.

[27] J. Massue, D. Frath, G. Ulrich, P. Retailleau, R. Ziessel, *Org. Lett.* **2012**, 14, 230–233.

[28] A. K. Chakraborti, S. Rudrawar, K. B. Jadhav, G.nKaur, S. V. Chankeshwara, *Green Chem.* **2007**, 9, 1335–1340.

[29] A. Altomare, M. C. Burla, M. Camalli, G. L. Cascarano, C. Giacovazzo, A. Guagliardi, A. G. G. Moliterni, G. Polidori, R. Spagna, *J. Appl. Cryst.* **1999**, 32, 115-119.

[30] G. M. Sheldrick, *Acta Cryst. C Struct. Chem.* **2015**, 71, 3–8.

[31] A. L. Spek, *Acta Cryst. D* **2009**, 65, 148–155.

[32] F. Neese, *Comput. Mol. Sci.* **2012**, 2, 73-78.

[33] J. P. Perdew, K. Burke, M. Ernzerhof, *Phys. Rev. Lett.* **1996**, 77, 3865–3868.

[34] J. P. Perdew, K. Burke, M. Ernzerhof, *Phys. Rev. Lett.* **1997**, 78, 1396–1396.

[35] A. Schäfer, H. Horn, R. Ahlrichs, *J. Chem. Phys.* **1992**, 97, 2571–2577.

[36] A. Schäfer, C. Huber, R. Ahlrichs, *J. Che.m Phys.* **1994**, 100, 5829–5835.

[37] F. Weigend, R. Ahlrichs, *Phys. Chem. Chem. Phys*. **2005**, 7, 3297–3305.

[38] S. Grimme, J. Antony, S. Ehrlich, H. Krieg, *J. Chem. Phys.* **2010**, 132, 154104.

[39] S. Grimme, S. Ehrlich, L. Goerigk, *J. Comput. Chem.* **2011**, 32, 1456–1465.

[40] R. Izsák, F. Neese, W. Klopper, *J. Chem. Phys.* **2013**, 139, 094111.

[41] R. Izsák, F. Neese, *J. Chem. Phys.* **2011**, 135, 144105.

[42] S. Grimme, F. Neese, *J. Chem. Phys.* **2007**, 127, 154116.

[43] Www.Chemcraftprog.Com.

[44] C. Wyman, P. Sloan, P. Shirley, *J. of Comp. Graph. Tech. (JCGT)* **2013**, 2, 1-11.

[45] Y. Tian, X. Xu, J. Wang, C. Yao, L. Li, *ACS Appl. Mater. Inter.* **2014**, 6, 8631–8638.

[46] G. E. Nunes, A. L. Sehnem, I. H. Bechtold, *Liq. Cryst.* **2012**, 39, 205–210.